Wave propagation through saturated porous media

I. Malinouskaya*
LCD, SP2MI, BP 30179, 86962 Futuroscope Cedex, UPMC Sisyphe. Boîte 105, 4 place Jussieu, 75252 Paris cedex 05, France

V. V. Mourzenko† and J.-F. Thovert‡
LCD, SP2MI, Boîte Postale 30179, 86962 Futuroscope Cedex, France

P. M. Adler§
UPMC Sisyphe. Boîte 105, 4 place Jussieu, 75252 Paris cedex 05, France
(Received 4 January 2008; published 5 June 2008)

The homogenization procedure is applied to the problem of wave propagation in the biphasic mode in porous media saturated with a Newtonian fluid. The local problems corresponding to the solid and fluid phases have been solved separately for complex three-dimensional media. The effective rigidity tensor, some effective coefficients, the dynamic permeability, the celerities, and the attenuation of the three waves are systematically determined. The characteristic length Λ was successfully used to gather results for the dynamic permeability as well as for the attenuation coefficients for all media.

DOI: 10.1103/PhysRevE.77.066302 PACS number(s): 47.56.+r, 61.43.Gt, 62.65.+k, 43.20.+g

I. INTRODUCTION

Wave propagation through saturated porous media is of large theoretical and practical interest. In seismic prospection, for instance, in most cases waves propagate through media which contain at least one fluid and often two such as oil or water. The presence of these fluids influences the wave celerities.

The first study of wave propagation on the macroscopic level in saturated porous media is the poroelasticity theory of [1] for low frequencies which was extended by [2] for any frequency range. Suppose that the elastic solid matrix is saturated with a compressible viscous fluid and that the solid and fluid densities are comparable. Macroscopic parameters such as the effective elastic moduli of the solid skeleton, its compressibility, and its permeability are required in this approach. Two propagation modes are found which depend on the frequency range. The low frequencies correspond to the drained regime for which the relative fluid and solid motion is not zero, while the high frequencies correspond to the undrained regime.

In the first mode, Ref. [2] demonstrated that two types of waves propagate in the saturated media. The first one is the fast compressional and shear waves, which correspond to waves propagating in the elastic solid. The second one is the slow compressional wave characterized by an important attenuation, which was observed for the first time by [3].

In contrast with the macroscopic analysis of [2], the homogenization method derives the macroscopic properties from the local characteristics of the media. This approach was used by [4] for the quasistatic case and by [5] and [6] for the dynamic behavior.

Reference [7] used the homogenization procedure in order to study the harmonic wave propagation in porous media saturated with a viscous Newtonian incompressible fluid. There are three possible modes of wave propagation depending on the order of the transient Reynolds number: namely, the biphasic, elastic, and viscoelastic modes. These modes are also related to the contrast between mechanical properties of the solid and fluid. Generally speaking, this method requires the solution of the elastic equations in the solid and of the Navier-Stokes equation in the fluid; the first problem is the same as for dry media.

The influence of the frequency and geometric characteristics on the dynamic permeability was examined by [8] and [9] for various frequency ranges. The dynamic permeability which requires the solution of the Navier-Stokes equation depends on the frequency, and for simple geometries it can be obtained analytically [2]. Reference [8] demonstrated that the dynamic permeability can be expressed as a function of the static permeability and the length scale for tube networks. Other geometries such as rough channels were examined by [10]. We are not aware of any contribution for complex random geometries.

The major objective of our work is to study wave propagation in dry or saturated media. For dry media, the wave celerities, the polarization correction, the dispersion, and the attenuation are reported in the companion paper [11]. The present paper studies in a systematic way the dynamic permeability and the celerities of the various waves in saturated porous media with realistic and real geometries. The overlap between the two papers has been reduced to a minimum and is restricted to the necessary common material in the general presentation; there is no overlap in terms of results.

Section II recalls the basic equations which govern these phenomena and the main features of the methodology which is employed to solve them. Section III presents the biphasic macroscopic mode which will be studied in most part of this paper when both solid and liquid phases influence the macroscopic wave properties.

*malinoui@ensma.fr
†murzenko@lcd.ensma.fr
‡thovert@lcd.ensma.fr
§pierre.adler@upmc.fr

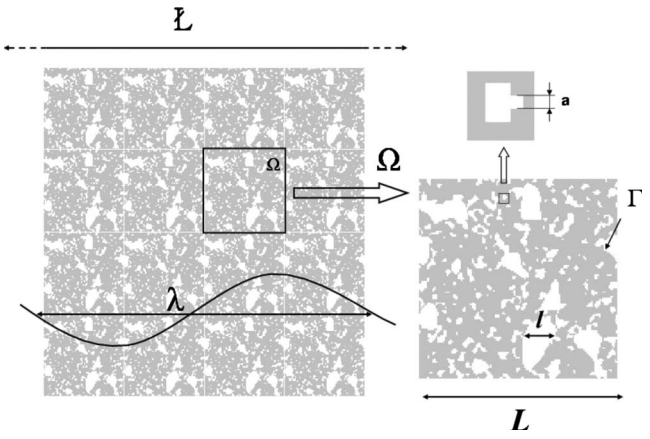

FIG. 1. Length scales in Eq. (2). The periodic medium is composed of identical unit cells Ω. Internal free boundaries are denoted by Γ.

The dynamic permeability is detailed in Sec. IV. The numerical solution is briefly commented on, but this section is mostly devoted to the results obtained for a few types of reconstructed media and to two real samples measured by microtomography. Several dimensionless representations are tried based on the choice of various length scales.

The elastic problem which was already partly studied in [11] is presented in Sec. V. The celerities of the three waves and their attenuations are given in Sec. VI for the various media which were detailed in Sec. IV. Again various dimensionless representations are discussed. Finally, the results are summarized in Sec. VII.

Technical details are gathered in [12] available at the Electronic Physics Auxiliary Service. It is divided into two parts; the first one presents the solution of the microscopic equations and the resulting macroscopic quantities; the second one presents the necessary developments for the elastic problem posed by a solid medium saturated with a fluid.

II. GENERAL

A. Basic equations

The porous matrix is an elastic heterogeneous material. The size l of the heterogeneities (scale of the geometrical microstructure or of property variations) is supposed to be much smaller than the overall dimension Ł of the domain (Fig. 1). The material is assumed to be statistically homogeneous on some intermediate scale between l and Ł, and therefore it can be regarded as spatially periodic; i.e., it is made of identical unit cells Ω of size L. Ω is partitioned into a solid and a fluid phase denoted by Ω_s and Ω_f, respectively. Ω_f is filled by an incompressible Newtonian fluid.

Consider the propagation in this medium of an harmonic wave of pulsation ω and wavelength λ intermediate between l and Ł. In the following, the length $\mathcal{L}$ is used as a characteristic macroscopic scale:

$$\mathcal{L} = \lambda/2\pi. \tag{1}$$

Moreover, the lengths l, L, $\mathcal{L}$, and λ verify

$$l \leq L \ll \mathcal{L} = \lambda/2\pi. \tag{2}$$

The small parameter η, which is going to play a key role in the expansion of the solution [13], is defined as

$$\eta = l/\mathcal{L} \ll 1. \tag{3}$$

Hereafter, all the quantities relative to the solid and fluid phases are denoted by the subscripts s and f. ρ, $\boldsymbol{u}$, and $\boldsymbol{\sigma}$ denote the density, displacement, and stress tensor of the two materials, respectively. The displacements $\boldsymbol{u}_s$ and $\boldsymbol{u}_f$ are of the form

$$\boldsymbol{u} = \hat{\boldsymbol{u}} e^{i\omega t}. \tag{4}$$

In the solid matrix Ω_s, wave propagation is governed on the microscopic level by the elastic equation

$$\nabla \cdot \boldsymbol{\sigma}_s = -\rho_s \omega^2 \boldsymbol{u}_s \quad \text{in } \Omega_s, \tag{5a}$$

where

$$\boldsymbol{e} = [\nabla \cdot \boldsymbol{u}_s + (\nabla \cdot \boldsymbol{u}_s)^t]/2, \quad \boldsymbol{\sigma}_s = \boldsymbol{C}_{\{4\}} : \boldsymbol{e}, \tag{5b}$$

where $\boldsymbol{C}_{\{4\}}$ is the solid fourth-order elastic tensor. For isotropic materials, the expression of the stress tensor reduces to

$$\boldsymbol{\sigma}_s = \lambda_s (\mathrm{tr}\, \boldsymbol{e}) + 2\mu_s \boldsymbol{e}, \tag{5c}$$

where λ_s and μ_s are the Lamé coefficients.

The fluid velocity $\boldsymbol{V}$ is given by

$$\boldsymbol{V} = \frac{\partial \boldsymbol{u}_f}{\partial t} = i\omega \boldsymbol{u}_f. \tag{6}$$

Therefore, the linearized Navier-Stokes equations for the fluid motion in Ω_f can be written

$$\nabla \cdot \boldsymbol{\sigma}_f = \rho_f \omega \boldsymbol{V}, \quad \nabla \cdot \boldsymbol{V} = 0, \tag{7}$$

together with

$$\boldsymbol{\sigma}_f = -P\boldsymbol{I} + 2\mu_f \boldsymbol{\mathcal{D}}(\boldsymbol{V}), \quad \boldsymbol{\mathcal{D}}(\boldsymbol{V}) = \frac{1}{2}(\nabla \cdot \boldsymbol{V} + {}^t\nabla \cdot \boldsymbol{V}), \tag{8}$$

where P is the pressure and μ_f the dynamic viscosity.

Continuity of displacements and normal stresses at the solid-fluid interface Γ implies

$$\boldsymbol{u}_s = \boldsymbol{u}_f, \quad (\boldsymbol{\sigma}_s - \boldsymbol{\sigma}_f) \cdot \boldsymbol{n} = 0 \quad \text{on } \Gamma, \tag{9}$$

where $\boldsymbol{n}$ is the unit normal to Γ.

B. Double-scale expansion in periodic heterogeneous media

In order to distinguish between the macroscopic and microscopic scales, two spatial variables $\boldsymbol{x}$ and $\boldsymbol{y}$ are introduced. $\boldsymbol{x}$ is macroscopic—i.e., of order $\mathcal{L}$—while $\boldsymbol{y}$ is microscopic—i.e., of order l. Therefore,

$$\boldsymbol{y} = \eta^{-1} \boldsymbol{x}. \tag{10}$$

Consequently, the spatial gradient operator becomes

$$\nabla = \nabla_x + \eta^{-1} \nabla_y, \tag{11}$$

where ∇_x and ∇_y are differential operators with respect to the variables $\boldsymbol{x}$ and $\boldsymbol{y}$, respectively. Any function of space can be

represented as a function of these variables, $\boldsymbol{f}(\boldsymbol{x},\boldsymbol{y})$. Because of the spatial periodicity of the medium, $\boldsymbol{f}$ is periodic in $\boldsymbol{y}$; moreover, $\boldsymbol{f}$ can be expanded as a series in terms of η:

$$\boldsymbol{f}(\boldsymbol{x},\boldsymbol{y}) = \sum \eta^j \boldsymbol{f}^{(j)}(\boldsymbol{x},\boldsymbol{y}), \tag{12}$$

where $\boldsymbol{f}^{(j)}(\boldsymbol{x},\boldsymbol{y})$ is also a periodic function of $\boldsymbol{y}$.

This expansion is applied to the displacements $\boldsymbol{u}_s$ and $\boldsymbol{u}_f$ and the pressure P:

$$\boldsymbol{u}_s(\boldsymbol{x},\boldsymbol{y},t) = \sum \eta^j \boldsymbol{u}_s^{(j)}(\boldsymbol{x},\boldsymbol{y},t), \tag{13a}$$

$$\boldsymbol{u}_f(\boldsymbol{x},\boldsymbol{y},t) = \sum \eta^j \boldsymbol{u}_f^{(j)}(\boldsymbol{x},\boldsymbol{y},t), \tag{13b}$$

$$P(\boldsymbol{x},\boldsymbol{y},t) = \sum \eta^j P^{(j)}(\boldsymbol{x},\boldsymbol{y},t), \tag{13c}$$

where P, $\boldsymbol{u}_s$, and $\boldsymbol{u}_f$ are periodic functions of $\boldsymbol{y}$.

Substitution of this expansion of $\boldsymbol{u}_s$, Eq. (13a), into Eq. (5a) yields expansions for the deformation operator $\boldsymbol{e}$ and the stress tensor $\boldsymbol{\sigma}_s$. Then, a series of equations for the solid phase for each power of η is obtained:

$$\eta^{-2}{:}\nabla_y \cdot \boldsymbol{\sigma}_s^{(-1)} = 0,$$

$$\eta^{-1}{:}\nabla_y \cdot \boldsymbol{\sigma}_s^{(0)} + \nabla_x \cdot \boldsymbol{\sigma}_s^{(-1)} = 0,$$

$$\eta^{0}{:}\nabla_y \cdot \boldsymbol{\sigma}_s^{(1)} + \nabla_x \cdot \boldsymbol{\sigma}_s^{(0)} = -\rho_s \omega^2 \boldsymbol{u}_s^{(0)},$$

$$\ldots,$$

$$\eta^{j}{:}\nabla_y \cdot \boldsymbol{\sigma}_s^{(j+1)} + \nabla_x \cdot \boldsymbol{\sigma}_s^{(j)} = -\rho_s \omega^2 \boldsymbol{u}_s^{(j)}. \tag{14}$$

The expansion (13a)–(13c) of $\boldsymbol{u}_f$ implies

$$\boldsymbol{V}(\boldsymbol{x},\boldsymbol{y},t) = \sum \eta^j \boldsymbol{V}^{(j)}(\boldsymbol{x},\boldsymbol{y},t), \tag{15}$$

with $\boldsymbol{V}^{(j)} = i\omega \boldsymbol{u}_f^{(j)}$; $\boldsymbol{V}^{(j)}$ is Ω periodic. Similarly, the stress tensor $\boldsymbol{\sigma}_f$ can be expanded as

$$\boldsymbol{\sigma}_f = \sum_{j=-1}^{\infty} \eta^j \boldsymbol{\sigma}_f^{(j)}. \tag{16}$$

Substitution of the expansions (15) and (16) into Eq. (7) yields a series of equations for the fluid phase similar to that for the solid one for each power of η:

$$\eta^{-2}{:}\nabla_y . \cdot \boldsymbol{\sigma}_f^{(-1)} = 0,$$

$$\eta^{-1}{:}\nabla_y \cdot \boldsymbol{\sigma}_f^{(0)} + \nabla_x \cdot \boldsymbol{\sigma}_f^{(-1)} = 0,$$

$$\eta^{0}{:}\nabla_y \cdot \boldsymbol{\sigma}_f^{(1)} + \nabla_x \cdot \boldsymbol{\sigma}_f^{(0)} = \rho_f i\omega \boldsymbol{V}^{(0)}, \tag{17}$$

$$\ldots,$$

$$\eta^{j}{:}\nabla_y \cdot \boldsymbol{\sigma}_f^{(j+1)} + \nabla_x \cdot \boldsymbol{\sigma}_f^{(j)} = \rho_f i\omega \boldsymbol{V}^{(j)},$$

$$\nabla_y \cdot \boldsymbol{V}^{(0)} = 0,$$

$$\nabla_y \cdot \boldsymbol{V}^{(j+1)} + \nabla_x \cdot \boldsymbol{V}^{(j)} = 0, \quad j = 1,2,3,\ldots. \tag{18}$$

The rate of deformation $\boldsymbol{\mathcal{D}}$ can be derived from Eq. (15) as

$$\boldsymbol{\mathcal{D}}(\boldsymbol{V}) = \eta^{-1}\boldsymbol{\mathcal{D}}_y(\boldsymbol{V}^{(0)}) + \sum_{j=0}^{\infty} \eta^j [\boldsymbol{\mathcal{D}}_x(\boldsymbol{V}^{(j)}) + \boldsymbol{\mathcal{D}}_y(\boldsymbol{V}^{(j+1)})], \tag{19}$$

where $\boldsymbol{\mathcal{D}}_x$ and $\boldsymbol{\mathcal{D}}_y$ denote the operator $\boldsymbol{\mathcal{D}}$ applied to the variables $\boldsymbol{x}$ and $\boldsymbol{y}$, respectively.

Finally, the conditions for each power of η at the solid-fluid interface are

$$\boldsymbol{u}_s^{(j)} = \boldsymbol{u}_f^{(j)}, \quad (\boldsymbol{\sigma}_s^{(j)} - \boldsymbol{\sigma}_f^{(j)}) \cdot \boldsymbol{n} = 0 \quad \text{on } \Gamma. \tag{20}$$

C. Various modes of wave propagation in a saturated porous medium

By its macroscopic analysis, Ref. [2] showed that there are two propagation modes for the low- and high-frequency ranges. Similarly, by the homogeneization approach, Ref. [7] showed that a transient Reynolds number R_T appears in the dimensionless flow Eq. (7):

$$R_T = \frac{\rho_f \omega l^2}{\mu_f}. \tag{21}$$

Three different modes of wave propagation are found for $R_T = O(1)$, $O(\eta)$, and $O(\eta^2)$. These modes are also related to the contrast $\mu_f \omega / \|\boldsymbol{C}_{\{4\}}\|$ between the mechanical properties $\boldsymbol{C}_{\{4\}}$ of the solid and $\mu_f \omega$ of the fluid, which can be of the order $O(\eta^2)$, $O(\eta)$, and $O(1)$.

Since the small parameter η is proportional to the ratio between the microscale l and the wavelength λ, it is proportional to the frequency ω:

$$\eta \sim l\omega \sqrt{\frac{\rho_f}{E_s}}, \tag{22}$$

where E_s is the Young's modulus of the solid.

1. Biphasic macroscopic mode

A Reynolds number of order $O(1)$ corresponds to the low-frequency range studied by [2]. The contrast between mechanical properties of the solid and fluid is of order $O(\eta^2)$. Then, the stress tensor $\boldsymbol{\sigma}_f$ takes the form

$$\boldsymbol{\sigma}_f = -\boldsymbol{I}P + \eta^2 2\mu_f \boldsymbol{\mathcal{D}}(\boldsymbol{V}). \tag{23}$$

Substitution of Eqs. (15), (13c), and (19) into Eq. (23) yields an expansion for $\boldsymbol{\sigma}_f$, Eq. (16), as

$$\boldsymbol{\sigma}_f^{(-1)} = 0,$$

$$\boldsymbol{\sigma}_f^{(0)} = -\boldsymbol{I}P^{(0)},$$

$$\boldsymbol{\sigma}_f^{(1)} = -\boldsymbol{I}P^{(1)} + 2\mu_f \boldsymbol{\mathcal{D}}_y(\boldsymbol{V}^{(0)}),$$

$$\ldots,$$

$$\boldsymbol{\sigma}_f^{(j)} = -\boldsymbol{I}P^{(j)} + 2\mu_f [\boldsymbol{\mathcal{D}}_x(\boldsymbol{V}^{(j-2)}) + \boldsymbol{\mathcal{D}}_y(\boldsymbol{V}^{(j-1)})] \quad (j > 1). \tag{24}$$

In this case, the wave celerity depends on the global characteristics of both phases [7]. Thus, this macroscopic mode is

called biphasic or equivalently drained since the relative fluid and solid motion is not zero. This mode, which represents the most general situation, is the one which is going to be studied.

2. Elastic macroscopic mode

The transient Reynolds number $R_T=O(\eta)$ corresponds to the high-frequency range studied by [2]. The contrast between the fluid and solid mechanical characteristics $\mu_f\omega$ and $\boldsymbol{C}_{\{4\}}$ is of the same order of magnitude as R_T—i.e., $\mu_f\omega/\|\boldsymbol{C}_{\{4\}}\|=O(\eta)$.

Since this mode can be derived from the biphasic mode by equating the fluid and solid displacements $\boldsymbol{u}_f^{(0)}$ and $\boldsymbol{u}_s^{(0)}$, no further details are given. However, it is worth mentioning that in contrast with the biphasic mode, there is no relative fluid and solid motion and this regime can be also called the undrained regime.

3. Viscoelastic macroscopic mode

The third mode of wave propagation obtained by [7] corresponds to very high frequencies when the transient Reynolds number R_T is of order $O(\eta^2)$. The contrast between the fluid and solid mechanical characteristics $\boldsymbol{C}_{\{4\}}$ and $\mu_f\omega$ is small. Since these very high frequencies do not correspond to acoustic waves, this mode will not be studied here. The Navier-Stokes equation keeps its form (7) and (8), and on a macroscopic scale, the medium behaves as a monophasic and viscoelastic material (for more details, see [7]).

III. BIPHASIC MACROSCOPIC MODE OF A SATURATED POROUS MEDIUM

Wave propagation follows the biphasic macroscopic behavior if

$$\frac{\omega\rho_f l^2}{\mu_f}=O(1),\quad \frac{\mu_f\omega}{\|\boldsymbol{C}_{\{4\}}\|}=O(\eta^2). \tag{25}$$

The macroscopic description can be obtained from the fluid and solid microscopic equations with the appropriate conditions at the solid-fluid interface. The detailed developments, which follow closely [7], are given in Sec. A of [12]. The asymptotic expansion for the pressure and for the displacement fields and the introduction of two scales allows us to derive the governing equations for the fluid and solid phases at various orders in η. Considering them successively, two separate problems for micro- and macroscales are obtained. The macroscopic description is derived by integration of the microscopic equations over Ω_s for the solid and over Ω_f for the fluid, respectively. The coefficients for the macroscopic equations (A44) of [12] are determined by solving two problems in the solid and in the fluid phases.

The linearized Navier-Stokes equation in terms of the relative velocity $\boldsymbol{\mathcal{W}}$, Eq. (A26), reads as

$$\mu_f\Delta_y\boldsymbol{\mathcal{W}}-i\rho_f\omega\boldsymbol{\mathcal{W}}-\nabla_y P^{(1)}=-\boldsymbol{G},\ \nabla_y\cdot\boldsymbol{\mathcal{W}}=0\ \text{in}\ \Omega_f, \tag{26a}$$

$$\boldsymbol{\mathcal{W}}=0\ \text{on}\ \Gamma,$$

from which the dynamic permeability $\boldsymbol{K}$ can be deduced:

$$(\boldsymbol{K}/\mu_f)\cdot\boldsymbol{G}=\langle\boldsymbol{\mathcal{W}}\rangle. \tag{26b}$$

This equation describes the wave propagation at frequency ω in the fluid. It corresponds to the fluid motion submitted to the macroscopic pressure gradient $\boldsymbol{G}$.

The effective stiffness tensor $\boldsymbol{D}_{\{4\}}^{(0)}$ can be determined from the solution of the elastostatic equation when the porous medium is submitted to the macroscopic deformation $\boldsymbol{E}(\boldsymbol{U}^{(0)})$:

$$\nabla_y\cdot\{\boldsymbol{C}_{\{4\}}:[\boldsymbol{e}(\boldsymbol{u}^{(1)})+\boldsymbol{E}(\boldsymbol{U}^{(0)})]\}=0\quad\text{in}\ \Omega_s,$$

$$\{\boldsymbol{C}_{\{4\}}:[\boldsymbol{e}(\boldsymbol{u}^{(1)})+\boldsymbol{E}(\boldsymbol{U}^{(0)})]\}\cdot\boldsymbol{n}=0\quad\text{on}\ \Gamma. \tag{27a}$$

Therefore,

$$\boldsymbol{D}_{\{4\}}^{(0)}:\boldsymbol{E}(\boldsymbol{U}^{(0)})=\langle\boldsymbol{C}_{\{4\}}:[\boldsymbol{e}(\boldsymbol{u}^{(1)})+\boldsymbol{E}(\boldsymbol{U}^{(0)})]\rangle. \tag{27b}$$

The coefficients $\boldsymbol{\alpha}$ and β [Eqs. (A13) and (A14) in [12]], which quantify the mechanical reaction of the solid matrix on the fluid pressure, are derived from the solution of the elastostatic equation when the porous medium is submitted to the unit interstitial pressure $P=1$:

$$\nabla_y\cdot[\boldsymbol{C}_{\{4\}}:\boldsymbol{e}(\boldsymbol{q})]=0\quad\text{in}\ \Omega_s,\quad[\boldsymbol{C}_{\{4\}}:\boldsymbol{e}(\boldsymbol{q})]\cdot\boldsymbol{n}=-\boldsymbol{n}\quad\text{on}\ \Gamma. \tag{28a}$$

Therefore,

$$\boldsymbol{\alpha}=\langle\boldsymbol{C}_{\{4\}}:\boldsymbol{e}(\boldsymbol{q})\rangle,\quad\beta=\langle\nabla_y\cdot\boldsymbol{q}\rangle. \tag{28b}$$

The numerical solutions will be addressed in Sec. IV for the flow problem (26a) and (26b) and in Sec. V for the elastic problems (27a), (27b), (28a), and (28b).

IV. SOLUTION OF THE NAVIER-STOKES EQUATION: DYNAMIC PERMEABILITY

The full set of equations for the biphasic macroscopic description is given by (A44) in [12]. These equations are written for the unknowns $\boldsymbol{U}^{(0)}$, $\langle\boldsymbol{W}\rangle$, and $P^{(0)}$. The coefficients $\boldsymbol{D}_{\{4\}}^{(0)}$, $\boldsymbol{\alpha}$, β, and $\boldsymbol{K}$ are the macroscopic characteristics derived from the solutions of the local problems (27a), (27b), (28a), (28b), (26a), and (26b), which can be solved separately.

The dynamic permeability $\boldsymbol{K}$ is a frequency-dependent tensor with complex values

$$\boldsymbol{K}=\boldsymbol{K}_r+i\boldsymbol{K}_i,\quad\boldsymbol{K}_r=\mathrm{Re}(\boldsymbol{K}),\quad\boldsymbol{K}_i=\mathrm{Im}(\boldsymbol{K}). \tag{29}$$

The meaning of the complex values of $\boldsymbol{K}$ can be grasped by considering the simple case of an isotropic permeability tensor:

$$\boldsymbol{K}=K\boldsymbol{I},\quad K=K_r+iK_i. \tag{30}$$

Then, the dynamic Darcy's law (A36) in [12] can be written as

$$\langle\mathcal{W}\rangle=\mu_f^{-1}|K|(-\nabla_x\cdot P^{(0)}+\rho_f\omega^2\boldsymbol{U}_s^{(0)})e^{i\arctan(K_i/K_r)}. \tag{31}$$

The ratio K_i/K_r characterizes the phase change of the propagating wave. As shown by [2], when ω increases, $|K|$ de-

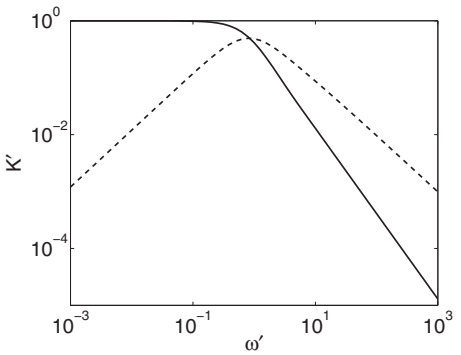

FIG. 2. The analytical solution for the dynamic permeability given by [2] for a porous medium of porosity ϵ made of parallel-plane channels of aperture $2h$. K' and ω' are the dimensionless permeability and frequency, $K'=3K/(\epsilon h^2)$, and $\omega'=h^2\omega/(3\nu_f)$. Solid line: Re$(K')$. Dashed line: $-$Im(K').

creases and $|K_i|$ becomes larger than $|K_r|$; i.e., the phase shift increases and influences the wave amplitude, which is decreased. On the other hand, when ω tends to zero, K tends to the static permeability and the phase shift disappears (Fig. 2).

A. Problem formulation

The Navier-Stokes equation for the incompressible fluid submitted to the pressure gradient ∇P is written as

$$\mu_f \Delta \boldsymbol{\mathcal{W}} - i\rho_f \omega \boldsymbol{\mathcal{W}} = \nabla P, \quad \nabla \cdot \boldsymbol{\mathcal{W}} = 0 \quad \text{in } \Omega_f,$$
$$\boldsymbol{\mathcal{W}} = 0 \quad \text{on } \Gamma, \tag{32}$$

where $\boldsymbol{\mathcal{W}}$ is the fluid velocity and P the pressure, which can be decomposed into a linear trend associated with a macroscopic pressure gradient $-\boldsymbol{G}$ and Ω-periodic fluctuations $\tilde{P}$:

$$P = -\boldsymbol{y} \cdot \boldsymbol{G} + \tilde{P}. \tag{33}$$

The introduction of Eq. (33) into Eq. (32) yields a microscopic fluid equation of order $O(\eta^0)$:

$$\mu_f \Delta \boldsymbol{\mathcal{W}} - i\rho_f \omega \boldsymbol{\mathcal{W}} = -\boldsymbol{G} + \nabla \tilde{P}, \quad \nabla \cdot \boldsymbol{\mathcal{W}} = 0 \quad \text{in } \Omega_f,$$
$$\boldsymbol{\mathcal{W}} = 0 \quad \text{on } \Gamma. \tag{34}$$

Therefore, $\tilde{P}$ corresponds to the field $P^{(1)}$ in Eq. (26a). The components of $\boldsymbol{K}$ can be obtained by solving Eq. (34) for a unit gradient $\boldsymbol{G}$ along each direction x, y, and z [see Eq. (26b)]. For an isotropic medium, K, Eq. (30), is derived from the solution of Eq. (34) for any $\boldsymbol{G}$.

B. Numerical solution

Define the dimensionless quantities denoted by a prime:

$$P = P' P_0, \quad \nabla = \nabla' \frac{1}{l}, \quad \Delta = \Delta' \frac{1}{l^2}, \quad \boldsymbol{\mathcal{W}} = \boldsymbol{\mathcal{W}}' \mathcal{W}_0,$$
$$\omega = \omega' \omega_0, \quad \boldsymbol{G} = \frac{P_0}{l} \boldsymbol{G}', \tag{35}$$

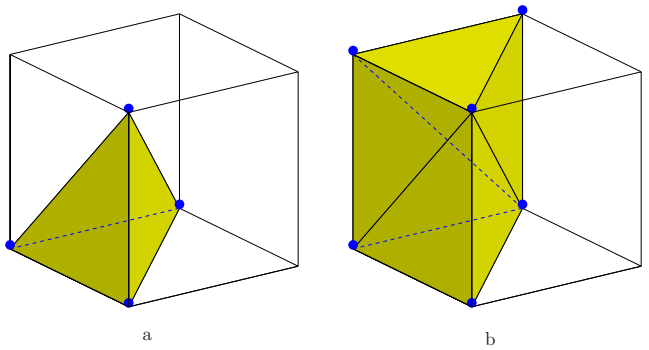

FIG. 3. (Color online) The structured mesh SCT_6. The domain is represented by a regular array of cubic elements. Each of them is decomposed into six identical tetrahedra; one of them is shown in (a) and three of them in (b) where one of the symmetry planes is visible.

where l is the characteristic length scale and P_0, $\mathcal{W}_0$, and ω_0 are characteristic values of the pressure P, velocity $\boldsymbol{\mathcal{W}}$, and frequency ω, respectively. By choosing

$$\mathcal{W}_0 = \frac{P_0 l}{\mu_f}, \quad \omega_0 = \frac{\mu_f}{\rho_f l^2}, \tag{36}$$

Eq. (34) becomes

$$\Delta' \boldsymbol{\mathcal{W}}' - i\omega' \boldsymbol{\mathcal{W}}' = -\boldsymbol{G}' + \nabla' \tilde{P}',$$
$$\nabla' \cdot \boldsymbol{\mathcal{W}}' = 0 \text{ in } \Omega_f, \quad \boldsymbol{\mathcal{W}}' = 0 \quad \text{on } \Gamma. \tag{37}$$

Note that ω' is equal to the Reynolds number R_T defined in Eq. (21). The solutions $\tilde{P}'$ and $\boldsymbol{\mathcal{W}}'$ are complex numbers, which can be written as

$$\boldsymbol{\mathcal{W}}' = \boldsymbol{\mathcal{W}}'_r + i\boldsymbol{\mathcal{W}}'_i, \quad \tilde{P}' = \tilde{P}'_r + i\tilde{P}'_i. \tag{38}$$

Substitute (38) into Eq. (37) to obtain

$$\Delta \boldsymbol{\mathcal{W}}'_r + \omega' \boldsymbol{\mathcal{W}}'_i = -\boldsymbol{G}' + \nabla' \tilde{P}'_r,$$
$$\Delta \boldsymbol{\mathcal{W}}'_i - \omega' \boldsymbol{\mathcal{W}}'_r = \nabla' \tilde{P}'_i \quad \text{in } \Omega_f, \tag{39a}$$

with

$$\nabla \cdot \boldsymbol{\mathcal{W}}'_r = \nabla \cdot \boldsymbol{\mathcal{W}}'_i = 0 \quad \text{in } \Omega_f, \quad \boldsymbol{\mathcal{W}}'_r = \boldsymbol{\mathcal{W}}'_i = 0 \quad \text{on } \Gamma. \tag{39b}$$

The numerical solution of the Eqs. (39a) and (39b) is based on a finite-volume formulation. The unknown velocities $\boldsymbol{\mathcal{W}}'_j$ and pressure $\tilde{P}'_j$ are determined at the grid points $\boldsymbol{r}_j$, which are the corners of a structured or unstructured tetrahedral mesh. In the present work, all the calculations have been made with the SCT_6-structured mesh defined and shown in Fig. 3 (see also [11]). The control volumes are parts of the tetrahedra Θ_k. Velocities and pressures are supposed to vary linearly over each tetrahedron. Therefore, their derivatives are piecewise constant and this numerical method is first order.

By integrating Eqs. (39a) over the control volume Ω_j, applying the divergence theorem, and using the discrete for-

mulation of the differential operators, the system of linear equations for $\mathcal{W}'_j$ is derived as

$$\boldsymbol{A}\cdot\boldsymbol{W}'=\boldsymbol{B}, \quad \text{where } \boldsymbol{W}'=\begin{pmatrix}\mathcal{W}'_r\\ \mathcal{W}'_i\end{pmatrix}, \tag{40}$$

where $\boldsymbol{B}$ is a forcing term that depends on $\tilde{P}'$.

The solution algorithm is as follows. First, for any initial field $\tilde{P}'_0$, the forcing term $\boldsymbol{B}_0$ is calculated; a classical conjugate-gradient algorithm is used to solve the system of linear Eqs. (40) for $\boldsymbol{W}'$ with $\boldsymbol{B}=\boldsymbol{B}_0$. Then, the artificial compressibility approach is used to determine the correction to $\tilde{P}'_0$ for the next iteration:

$$\tilde{P}'_{n+1}=\tilde{P}'_n+c_p^{-1}\nabla\cdot\boldsymbol{W}'_n, \quad n=0,1,\ldots, \tag{41}$$

where c_p is a pseudocompressibility coefficient which is first chosen arbitrarily and then adapted during numerical experiments to achieve stability during convergence. Then, $\boldsymbol{B}$ is recalculated and the corresponding corrections to $\boldsymbol{W}'$ are found. This algorithm is stopped when the residue estimated from the current pressure $\tilde{P}'_n$ and the residue estimated from the current velocity field $\boldsymbol{W}'$ are smaller than a prescribed solution accuracy ζ:

$$\frac{\|\tilde{P}'_{n+1}-\tilde{P}'_n\|}{\|\boldsymbol{G}'\|L}=\frac{\|c_p^{-1}\nabla\cdot\mathcal{W}'_n\|}{\|\boldsymbol{G}'\|L}\le\zeta, \quad \frac{\|\boldsymbol{A}\cdot\boldsymbol{W}'-\boldsymbol{B}\|}{\|\boldsymbol{B}\|}\le\zeta. \tag{42}$$

To quantify the computational requirements, consider the fluid flow motion in a cylindrical tube of radius $R=8$ within a cubic unit cell of size $L=30$ discretized by the SCT_6 mesh. The number of grid points in the pore space is $N_p=5910$, and the required memory is about 30 MB. The computational time T depends on ω'. For $\omega'\le O(1)$, T is about 30 s, while for $\omega'=10$ it is almost 2 min with a processor RISC Power4 1.5 GHz. Note that for more complicated geometries T significantly increases. For example, for a reconstructed porous medium of size 64 with a correlation length 8 and porosity $\epsilon=0.3$ (see Sec. IV C 1), the grid contains about 260 000 points and T is about 45 h for low values of ω'.

C. Results

In this section, the Navier-Stokes equation is solved for several model and real media and the function $\boldsymbol{K}(\omega')$ is determined.

1. Unimodal reconstructed porous media

Unimodal porous media are reconstructed according to prescribed porosity and correlation length. The details of the reconstruction procedure can be found in [14]. The sample is composed of elementary cubes of size a entirely filled with solid or void; this is described by a binary phase function $Z(\boldsymbol{x})$, which is equal to 1 if the point $\boldsymbol{x}$ belongs to the pore space and zero otherwise. This phase function is statistically

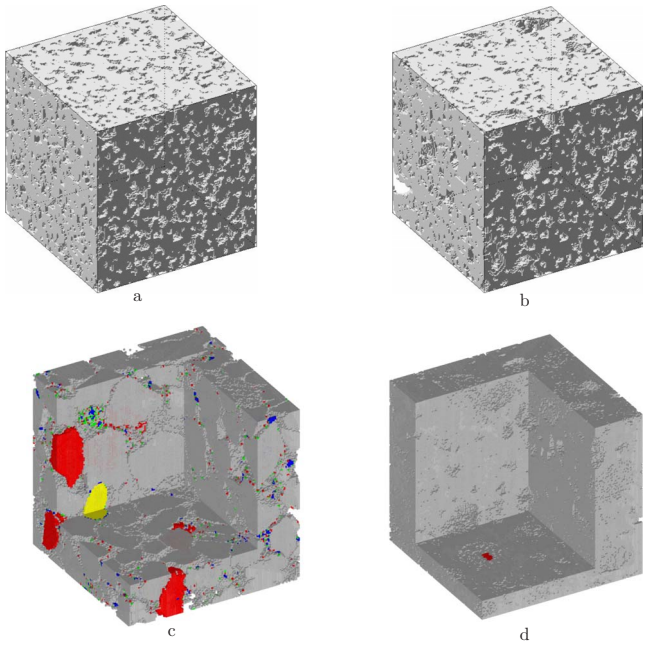

FIG. 4. (Color online) Model and real porous media discretized into 128^3 elementary cubes. (a) Unimodal medium HP. (b) Bimodal medium with nonpercolating vugs NPV; $\epsilon_p=0.24$ and $\epsilon_v=0.08$. (c) Real sandstone of size $L=716.8$ μm composed of five components; gray cubes are filled by quartz, red by K-feldspar, green by biotite, blue by pyrite, and yellow by zircon, respectively. (d) Real vuggy carbonate; gray and red cubes are filled by calcite and pyrite, respectively.

characterized by a porosity ϵ and a correlation function $R_Z(u)$:

$$\epsilon=\overline{Z(\boldsymbol{x})}, \quad R_Z(u)=\frac{\overline{[Z(\boldsymbol{x})-\epsilon][Z(\boldsymbol{x}+\boldsymbol{u})-\epsilon]}}{(\epsilon-\epsilon^2)}, \tag{43}$$

where u is the norm of the translation vector $\boldsymbol{u}$.

Here, $Z(\boldsymbol{x})$ is derived by thresholding standard Gaussian variables Y correlated by

$$R_Y(u)=e^{-u^2/l_c^2}, \tag{44}$$

where l_c is the correlation length.

Several samples of size $L=64a$ with different combinations (ϵ,l_c) were generated for the numerical experiments. Such a medium is illustrated in Fig. 4(a).

a. Influence of the correlation length. First, samples are studied with $\epsilon=0.3$ and $l_c/a=4,6,8,12,16,24,32$. A unit global pressure gradient $\boldsymbol{G}'$ is imposed along the x axis. The resulting vector $\langle\mathcal{W}'\rangle$ yields the components of the dimensionless permeability tensor $\boldsymbol{K}'=\boldsymbol{K}/l^2$:

$$\begin{pmatrix}K'_{xx}\\ K'_{xy}\\ K'_{xz}\end{pmatrix}=\langle\mathcal{W}'\rangle. \tag{45}$$

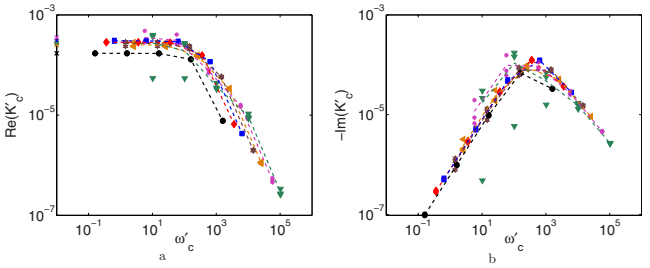

FIG. 5. (Color online) The real (a) and imaginary (b) parts of the permeability $K'_{xx,c}$ as functions of ω'_c for the unimodal media with $\epsilon=0.3$ and l_c/L equal to 1/16 (●), 3/32 (♦), 1/8 (■), 3/16 (★), 1/4 (◀), 3/8 (∗), and 1/2 (▼). The dashed lines correspond to the permeabilities $\bar{K}'_{xx,c}$ averaged over three independent realizations for each value of l_c; (×) is the corresponding static permeability.

Several length scales l will be used in the analysis of the data. When l is equal to l_c, denote

$$\boldsymbol{K}'_c = \boldsymbol{K}/l_c^2, \quad \omega'_c = \frac{\omega\rho_f l_c^2}{\mu_f}. \tag{46}$$

Note that all the media considered here are the same within changes in the observation scale; they should therefore yield identical $\boldsymbol{K}'$ for identical ω'. However, variations can be expected for two reasons. First, statistical fluctuations should be important when the statistical content of the sample is small—i.e., when l_c/L is of the order of unity. Second, systematic deviations may occur when the spatial discretization of the microstructure is poor—i.e., when l_c/a is not much larger than 1.

The averages $\bar{K}'_{xx,c}$ (generally denoted by an overbar) of $K'_{xx,c}$ over three independent realizations are displayed in Fig. 5. As expected, the data for $l_c/L=3/8$ and 1/2 are the most scattered because of the small statistical content. It is also observed that the results for the poorest discretization $l_c/a=4$ are noticeably smaller than the others.

$\mathrm{Re}(K'_{xx,c})$ [Fig. 5(a)] tend to their static values when ω'_c tends to zero, as expected. On the other hand, when $\omega'_c \to \infty$, $\mathrm{Re}(\bar{K}'_{xx,c})$ tend to zero as $(\omega'_c/\epsilon)^{-3/2}$ and $\mathrm{Im}(\bar{K}'_{xx,c})$ vary as $(\omega'_c/\epsilon)^{-3/4}$. For $\omega'_c \to 0$, $\mathrm{Im}(\bar{K}'_{xx,c})$ tend to zero as ω'_c.

The hydrodynamic properties of the media are primarily characterized by the absolute permeability. Two different modes are observed in Fig. 6(a) which correspond to the low- and the high-frequency ranges. In the first mode, $|K'_{xx,c}|$ is constant. Then, the behavior changes and $|K'_{xx,c}|$ tends to zero as $\omega'^{-3/4}$, since it is dominated by the imaginary part. It can be noticed that all the curves have similar shapes, but that they are shifted vertically; i.e., the onset frequency of the permeability decay varies.

In order to find a unified description for the permeability, let us use other length scales l. Ref. [15] proposed a characteristic length Λ, which is an intrinsic measure of the interconnected pore size. It is directly related to transport and can be defined as

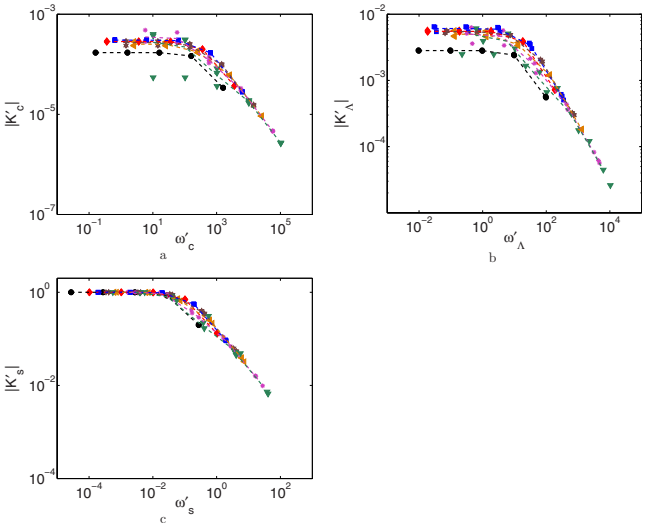

FIG. 6. (Color online) The modulus of the dimensionless permeabilities $|K'_c|$, $|K'_\Lambda|$, and $|K'_s|$ as functions of the frequencies (a) ω'_c, (b) ω'_Λ, and (c) ω'_s. Conventions are the same as in Fig. 5.

$$\Lambda = 2\frac{\displaystyle\int_{\Omega_f} \|\nabla\psi_0(\boldsymbol{r})\|^2 d^3\boldsymbol{r}}{\displaystyle\int_{\Gamma} \|\nabla\psi_0(\boldsymbol{r})\|^2 ds}. \tag{47}$$

Λ is calculated by solving the Laplace equation in the pore space [16].

The dimensionless permeability $\boldsymbol{K}'_\Lambda$ and frequency ω'_Λ are defined as [cf. Eq. (46)]

$$\boldsymbol{K}'_\Lambda = \boldsymbol{K}/\Lambda^2, \quad \omega'_\Lambda = \omega\rho_f\Lambda^2/\mu_f. \tag{48}$$

The average $|\bar{K}'_{xx,\Lambda}|$ over three independent realizations for each l_c is shown in Fig. 6(b). Λ reduces the scatter of the results for low frequencies, primarily by compensating for the statistical fluctuations for $l_c/L=3/8$ and 1/2.

Another characteristic length l_s which takes into account the transport properties of the medium can be derived from the static permeability K_0. With obvious notation,

$$l_s = \sqrt{K_0}, \quad \boldsymbol{K}'_s = \boldsymbol{K}/K_0, \quad \omega'_s = \omega\rho_f K_0/\mu_f. \tag{49}$$

This is very successful in gathering the data for all the correlation lengths. There is no scatter of the results in both limits $\omega'_s \to 0$ and $\omega'_s \to \infty$ and only residual fluctuations for the frequencies $\omega'=O(1)$ which correspond to the phase change of K_{xx}. For small ω'_s, the result is trivial because K is equal to K_o in this limit. However, this normalization isolates the dynamical effects which influence the permeability at large frequencies from the geometrical parameters which determine the static permeability.

b. Influence of porosity. The following series of tests has been done for unimodal media with $\epsilon=0.15$, 0.2, and 0.3 and $l_c/a=6$, 12, and 24. The sample size is still $L=64a$. Three independent realizations were again generated for each pair (ϵ, l_c) in order to estimate the statistical fluctuations. Note that the values $l_c/a=4$ and $l_c/a=32$, which yielded discreti-

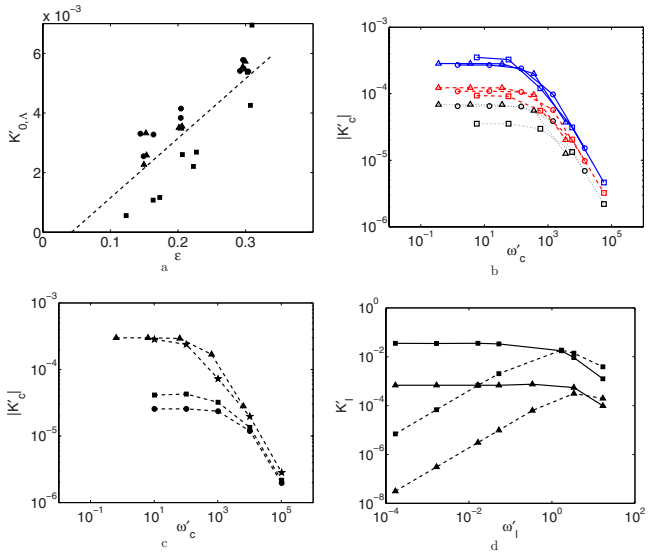

FIG. 7. (Color online) (a) The absolute permeability $K'_{0,\Lambda}$ as a function of porosity ϵ for unimodal media. Data are for $l_c/L=3/32$ (▲), 3/16 (●), and 3/8 (■). The dashed line corresponds to the numerical fit (50). (b),(c),(d) The modulus of the permeability $|\bar{K}'_{xx,c}|$ as a function of ω'_c. (b) Unimodal media. Data are for $\epsilon=0.15$ (black dotted line), 0.2 (red dashed line), and 0.3 (blue solid line); $l_c/L=3/32$ (△), 3/16 (○), and 3/8 (□). (c) Bimodal media; data are for HP (▲), NPV (●), PV (■), and HV (★). (d) Real media: sandstone (■) and carbonate (▲); the solid line corresponds to $\mathrm{Re}(K_{zz})/l^2$ and the dashed line to $-\mathrm{Im}(K_{zz})/l^2$ with $l=5.6$ μm.

zation effects and large statistical fluctuations, respectively, in the previous tests, are not used here.

The static permeability K_0, which is of course expected to be an increasing function of ϵ and l_c, can be approximated by [Fig. 7(a)]

$$\bar{K}'_{0,\Lambda}=\bar{K}_0/\Lambda^2=0.02\epsilon-8.5\times10^{-4}. \tag{50}$$

Note that this model predicts a percolation threshold for $\epsilon\approx0.0425$, which is consistent with the observations of [17] for Fontainebleau sandstones.

Let us now examine the behavior of the dynamic permeability $\bar{K}_{xx}$ averaged over three independent realizations for each pair (ϵ,l_c). Three sets of curves which correspond to the various values of ϵ are clearly distinguished in Fig. 7(b). In the low-frequency regime, their vertical shift results from the dependence of $\bar{K}'_{0,c}$ on ϵ. However, there is also a shift of the onset frequency for the permeability decay which increases when ϵ decreases.

The data were also normalized by Λ and K_0. This last choice, which is again the most successful, is displayed in Fig. 8(b).

2. Bimodal reconstructed porous media

Bimodal porous media possess micropores and macropores (also called vugs) with typical length scales l_p and l_v, respectively. They are reconstructed in two steps [18]. A first field $Z_p(\boldsymbol{x})$ with a porosity ϵ_p and a correlation length l_p which corresponds to the micropores is generated. Then, a

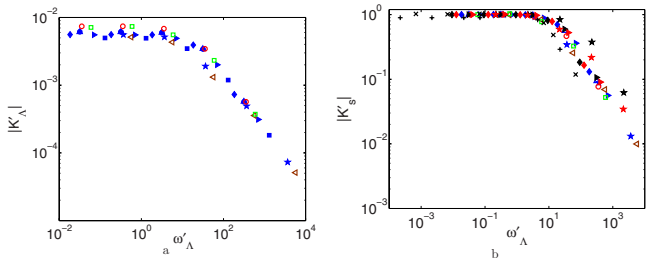

FIG. 8. (Color online) The dynamic permeabilities (a) $|K'_{zz,\Lambda}|$ and (b) $|K'_s|$ as functions of the frequency ω'_Λ. Data are for unimodal media: $l_c=6a$ (♦), $8a$ (●), $12a$ (▶), $16a$ (■), and $24a$ (★) with $\epsilon=0.15$ (black), $\epsilon=0.2$ (red), and $\epsilon=0.3$ (blue); bimodal media: HP (blue △), HV (brown ◁), NPV (red ○), and PV (green □); real media: vuggy carbonate (+) and sandstone (×).

second field $Z_v(\boldsymbol{x})$ statistically independent of $Z_p(\boldsymbol{x})$ is generated with a porosity ϵ_v and a correlation length l_v $(\gg l_p)$ which corresponds to the vugs. The bimodal medium is obtained by superposition of these two fields:

$$Z(\boldsymbol{x})=Z_p(\boldsymbol{x})+Z_v(\boldsymbol{x})-Z_p(\boldsymbol{x})Z_v(\boldsymbol{x}). \tag{51a}$$

The total porosity ϵ_t is derived by averaging the previous formula:

$$\epsilon_t=\epsilon_p+\epsilon_v-\epsilon_p\epsilon_v. \tag{51b}$$

Each of the two individual pore systems is statistically homogeneous on scales large with respect to l_p and l_v, and the bimodal porous medium itself is statistically homogeneous on scales larger than l_v. The unit cell is periodically reproduced in all directions.

Four media are used in this section. First, the sample named NPV (nonpercolating vugs) is characterized by $\epsilon_p=0.24$, $l_p=8a$, $\epsilon_v=0.08$, and $l_v=32a$. The second bimodal medium named PV (percolating vugs) is characterized by $\epsilon_p=0.167$, $l_p=8a$, $\epsilon_v=0.16$, and $l_v=32a$. For reference, a unimodal medium HP with micropores only $(\epsilon_p=0.3,\ l_p=8a)$ and a unimodal medium HV with vugs only $(\epsilon_v=0.3,\ l_v=32a)$ were also generated. All these samples have a size $L=128a$ and an overall porosity in the range 0.30–0.32. One sample is illustrated in Fig. 4(b).

$|K'_{zz}|$ normalized by l_v^2 for the samples with macroporosity (HV, PV, and NPV) and l_p^2 for the sample HP with microporosity only increases with ϵ_v [see Fig. 7(c)]. For the unimodal media HP and HV, which only differ by a scale change, the normalized data $|K'_{zz}|$ are indeed found to be nearly identical. The two bimodal media yield significantly smaller values of $|K'_{zz,c}|$, because ϵ_v associated with l_v is smaller and NPV does not even percolate by itself.

3. Real porous media

Two real samples were measured by microtomography. The first one is a sandstone of size $L=716.8$ μm with $\epsilon=0.246$, which is composed mostly of quartz and some k-feldspar, biotite, pyrite, and zircon. It is discretized by $(128)^3$ elementary cubes of size $a=5.6$ μm [see Fig. 4(c)].

$\boldsymbol{K}$ was calculated for ω ranging from 5 to 500 000 Hz. The pore space is filled by a brine with a viscosity $\mu_f=0.96$

$\times 10^{-3}$ Pa s and a density $\rho_f = 1.034 \times 10^3$ kg/m^3. The dimensionless frequency ω_c', Eqs. (35) and (36), is defined with l arbitrarily taken equal to 5.6 μm. The components of $\boldsymbol{K}$ are found by imposing a unit pressure gradient $\boldsymbol{G}$ along the z axis. Dimensionless values of the component K_{zz} are plotted in Fig. 7(d) as functions of ω_l'. Phase change occurs when $\omega_l' = O(1)$—i.e., $\omega \approx 10$ kHz.

The second medium is a vuggy carbonate which can be decomposed into 15% of pores, 84.84% of calcite, and 0.0175% of pyrite; it does not percolate along the x axis. L and the discretization of the sample are the same as before [Fig. 4(d)]. The calculations were performed for ω ranging from 5 to 500 000 Hz, with $\rho_f = 1.034 \times 10^3$ kg/m^3 and $\mu_f = 0.96 \times 10^{-3}$ Pa s.

A unit pressure gradient $\boldsymbol{G}$ is imposed along the z axis, and the dimensionless results are presented in Fig. 7(d), in comparison with sandstone. Since ρ_f, μ_f, and l are identical, this figure also provides a direct comparison of the dimensional permeabilities. The carbonate is found to be much less permeable than the sandstone, primarily because of its much smaller porosity. The offset frequency for the permeability decay is slightly larger. Again these results could be transposed to other fluids by setting the appropriate coefficients in Eq. (46).

4. Discussion

l_c is a natural choice for a comparison of unimodal media, and it is indeed sufficient for a fixed porosity. However, when several porosities associated with different typical sizes coexist and contribute differently to the hydraulic properties according to their volume fractions, it is difficult to predict which scale is the most relevant. This was illustrated in Fig. 7(c) for media with similar overall porosities, but different proportions of vugs and micropores.

It is therefore natural to use the length Λ, which is essentially a pore volume to pore surface ratio and thus a measure of the typical pore size; however, because of its definition Eq. (47), the pore regions which do or do not really contribute to a transport process are weighted by their volume. The data for unimodal and bimodal media with $\epsilon = 0.30$ are compared in Fig. 8(a), and they seem indeed to gather around a unique curve.

Another successful representation is $K_s'(\omega_s')$. It is not displayed for sake of brevity.

It is also possible to mix the length scales Λ and $\sqrt{K_0}$ as done in Fig. 8(b) with the plot $K_s'(\omega_\Lambda')$. The data include real and model media with ϵ ranging from 0.15 to 0.30. Again, this representation gathers fairly well the results.

The formation factor F is defined as the ratio between the electrical conductivities of the pore fluid σ_f and of the saturated porous medium σ when the solid phase is insulating:

$$F = \frac{\sigma_f}{\sigma}. \tag{52}$$

F is determined by solving the Laplace equation [14]. Λ and K_0 are approximately related to F for random networks of capillary tubes and channels [8]:

$$\frac{K_0 F}{\Lambda^2} = \frac{1}{8} \quad \text{for tubes,} \quad = \frac{1}{12} \quad \text{for channels.} \tag{53}$$

Different values have been obtained for other media, but of the same order of magnitude [16].

Because of Eq. (53), Λ^2 can be identified within a fairly constant factor with $K_0 F$ and Fig. 8(b) is equivalent to the representations of $|K_s'|$ vs $\omega \rho_f K_0 F / \mu_f$ used by [8], [9], and [10] for capillary networks, simple cubic lattices of solid grains, and corrugated channels, respectively. Therefore, our data extend these former results to more complex three-dimensional random geometries.

V. ELASTIC PROBLEMS

The macroscopic description of wave propagation in the biphasic mode requires the derivation of the rigidity tensor $\boldsymbol{D}_{\{4\}}^{(0)}$ from Eqs. (27a) and (27b) for imposed macroscopic deformations $\boldsymbol{E}(\boldsymbol{U}^{(0)})$ and the derivation of $\boldsymbol{\alpha}$ and β from Eqs. (28a) and (28b) for an imposed interstitial macroscopic pressure $P^{(0)}$. For clarity, the necessary developments are summarized in Sec. B of [12].

Since the results for $\boldsymbol{D}_{\{4\}}^{(0)}$ have been examined by [11], only the data for the coefficients $\boldsymbol{\alpha}$ and β are discussed here. If the solid matrix consists of nonoverlapping spheres such as in packed beds of spherical grains, β is given by

$$\beta_{gr} = -\frac{1-\epsilon}{K_s}, \tag{54}$$

where K_s is the solid bulk modulus. Moreover, an elementary analysis for a single spherical cavity in an unbounded solid matrix implies that β for a porous medium containing dilute spherical pores is given by (cf. Sec. B 3 in [12])

$$\beta_{cav} = -\frac{3\epsilon}{4\mu_s}, \quad \epsilon \ll 1. \tag{55}$$

It is interesting to note that for nonconsolidated media, which are analogous to the first case, β depends on K_s, while for consolidated media, which are analogous to the second case, β depends on μ_s.

Numerical calculations have been conducted for media made up of solid grains or containing spherical cavities, arranged in a simple cubic array, with ϵ ranging from 0.02 to 0.98. The results are shown in Fig. 9 and compared with Eqs. (54) and (55) for $\nu_s = 0.275$. For solid grains, an excellent agreement with Eq. (54) is observed, as long as $\epsilon \geq 1 - \frac{\pi}{6}$. For smaller porosities, the grains overlap and the situation progressively reverts to pores (first connected and then disconnected) in a consolidated material.

The numerical data for spherical pores agree with Eq. (55) up to $\epsilon = 0.05$. For larger porosities, Eq. (55) does not apply because of the interactions between cavities. Hence, β increases with ϵ more slowly than predicted by Eq. (55) and eventually starts decreasing when the cavities start overlapping for $\epsilon = \frac{\pi}{6}$. When ϵ approaches 1, only isolated solid parts remain and β is again given by Eq. (54), although these parts are not spherical.

Data for the uni- and bimodal media are also shown in Fig. 9, and the average value $\bar{\beta}$ was calculated for each pair

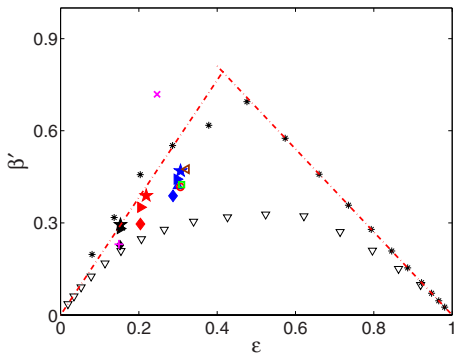

FIG. 9. (Color online) $\beta' = -\beta E_s$ for media containing spherical cavities (∇) or solid spheres ($*$), for the reconstructed porous media and for the real media; the dash-dotted red lines are the analytical solutions (55) for spherical cavities ($\epsilon \ll 1$) and (54) for solid spheres ($\epsilon > 1-\pi/6$). The Poisson ratio is $\nu_s = 0.275$ in all cases, except for the real media. Conventions are the same as in Fig. 8.

ϵ, l_c. All the data lie between the curves (54) and (55).

β' should be independent of l_c for a given porosity. Therefore, the differences in the numerical values can be viewed as a discretization effect.

Since all the media considered here are statistically isotropic or with a cubic symmetry, $\boldsymbol{\alpha}$ is related to β by

$$\boldsymbol{\alpha} = (\epsilon + \beta K_s)\boldsymbol{I}, \tag{56}$$

where K_s is the bulk modulus of the solid [12]. This relation has been successfully checked.

VI. MACROSCOPIC CHARACTERISTICS OF THE WAVE PROPAGATION: WAVE CELERITIES AND ATTENUATION

Once the dynamic hydrodynamic (Sec. IV) and elastic (Sec. V) properties are determined, the acoustic parameters can be derived. The displacement of the plane harmonic wave and the macroscopic pressure can be written as

$$\boldsymbol{u} = \tilde{\boldsymbol{u}} e^{(-ik\boldsymbol{x}\cdot\boldsymbol{p}+i\omega t)}, \quad P^{(0)} = \tilde{P}^{(0)} e^{(-ik\boldsymbol{x}\cdot\boldsymbol{p}+i\omega t)}, \tag{57}$$

where k is the wave number and $\boldsymbol{p}$ is the direction of the wave propagation. Using Eq. (57), the macroscopic Eqs. (A44) in [12] can be simplified; the wave celerities c and the vectors $\tilde{\boldsymbol{U}}_s^{(0)}$ and $\langle \tilde{\boldsymbol{W}} \rangle$ are found as the eigenvalues and the eigenvectors of the system

$$(\boldsymbol{B}^{-1}\cdot\boldsymbol{A})\cdot\boldsymbol{U} = c^2\boldsymbol{U} \quad \text{with} \quad \boldsymbol{U} = \begin{pmatrix} \tilde{\boldsymbol{U}}_s^{(0)} \\ \langle \tilde{\boldsymbol{W}} \rangle \end{pmatrix} \tag{58a}$$

and

$$\boldsymbol{A} = \begin{pmatrix} \boldsymbol{p}\cdot\boldsymbol{D}_{\{4\}}^{(0)}\cdot\boldsymbol{p} + \beta^{-1}\boldsymbol{p}\cdot\boldsymbol{\alpha}\boldsymbol{\alpha}\cdot\boldsymbol{p} & \beta^{-1}\boldsymbol{p}\cdot\boldsymbol{\alpha}\boldsymbol{p} \\ \dfrac{1}{\mu_f\beta}\boldsymbol{K}\cdot\boldsymbol{p}\boldsymbol{\alpha}\cdot\boldsymbol{p} & \dfrac{1}{\mu_f\beta}\boldsymbol{K}\cdot\boldsymbol{p}\boldsymbol{p} \end{pmatrix},$$

$$\boldsymbol{B} = \begin{pmatrix} \langle\rho\rangle\boldsymbol{I} & \langle\rho_f\rangle\boldsymbol{I} \\ -\dfrac{\rho_f}{\mu_f}\boldsymbol{K} & -\dfrac{i}{\omega}\boldsymbol{I} \end{pmatrix}. \tag{58b}$$

$\langle\cdots\rangle$ denotes the average operator over the unit cell [cf. (A15) in [12]]. Equations (58a) and (58b) can be further simplified for an isotropic medium. Consider first a shear wave with $\boldsymbol{U}_s^{(0)}$ and $\langle \boldsymbol{W} \rangle$ perpendicular to $\boldsymbol{p}$ and $\langle \boldsymbol{W} \rangle = W^* \boldsymbol{U}_s^{(0)}$. Taking into account (30) and (B5) in [12], the macroscopic Lamé coefficient $\mu_{s,eff}$ can be derived from Eqs. (58a) and (58b) as

$$\mu_{s,eff} = c_\perp^2(\langle\rho\rangle + \langle\rho_f\rangle W^*), \quad 0 = \frac{\rho_f}{i\omega\mu_f}K + W^*/\omega^2, \tag{59}$$

where $c_\perp$ is the shear wave celerity given by

$$c_\perp^2 = \frac{\mu_{s,eff}}{\langle\rho\rangle\left(1 - \dfrac{\langle\rho_f\rangle}{\langle\rho\rangle}\phi\right)}, \quad \phi = \frac{\omega\rho_f K}{i\mu_f}. \tag{60}$$

Similarly to Eq. (59), the macroscopic equation for the compressional wave can be simplified and a fourth-degree equation for $c_\parallel$ is derived as follows. The relative displacement $\langle \boldsymbol{W} \rangle$ which is parallel to $\boldsymbol{U}_s^{(0)}$ can be written as

$$\langle \boldsymbol{W} \rangle = W^* \boldsymbol{U}_s^{(0)}. \tag{61}$$

Taking into account (30) and (B5) in [12] and Eq. (61), Eq. (58a) and (58b) becomes

$$\lambda_{s,eff} + 2\mu_{s,eff} + \frac{\alpha^2}{\beta} - c_\parallel^2\langle\rho\rangle = W^*\left(c_\parallel^2\langle\rho_f\rangle - \frac{\alpha}{\beta}\right), \tag{62a}$$

$$\frac{\alpha}{\beta}\frac{K}{\mu_f} + c_\parallel^2\rho_f\frac{K}{\mu_f} = -W^*\left(\frac{1}{\beta}\frac{K}{\mu_f} + c_\parallel^2\frac{i}{\omega}\right). \tag{62b}$$

Denote by c_0 the compressional wave celerity for dry porous media ($\rho_f = 0$, $\mu_f = 0$),

$$c_0^2 = \frac{\lambda_{s,eff} + 2\mu_{s,eff}}{\langle\rho\rangle}, \tag{63}$$

and introduce the dimensionless parameters γ and ζ:

$$\gamma = \frac{\mu_f\beta c_0^2}{K\omega}, \quad \zeta = \frac{\rho_f}{\langle\rho\rangle}. \tag{64}$$

Then, using Eqs. (63) and (64), $c_\parallel$ is deduced by equating to zero the determinant of the eigenvalue problem Eqs. (62a) and (62b):

$$\left(\frac{c_\parallel}{c_0}\right)^4(\epsilon\langle\rho\rangle\beta\zeta^2c_0^2 - i\gamma) + \left(\frac{c_\parallel}{c_0}\right)^2\left(i\gamma\left\{1 + \frac{\alpha^2}{c_0^2\beta\langle\rho\rangle}\right\} - \{1 + \alpha\zeta(1+\epsilon)\}\right) + 1 = 0. \tag{65}$$

The two solutions of Eq. (65) correspond to the fast and slow compressional waves.

The celerities $c_\parallel$ for compressional and $c_\perp$ for shear waves are complex values—i.e.,

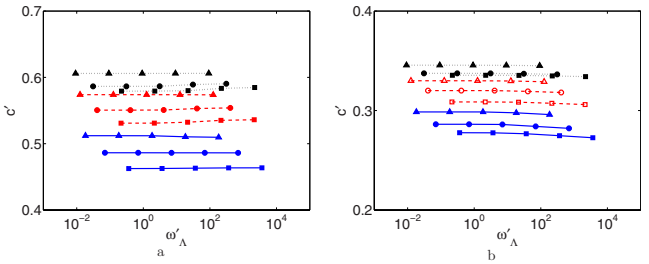

FIG. 10. (Color online) The compressional (a) and shear (b) wave celerities c' as functions of the frequency ω'_Λ for unimodal media. Data are for ϵ=0.15 (black dotted line), 0.2 (red dashed line), and 0.3 (blue solid line); l_c/L=3/32 (▲), 3/16 (●), and 3/8 (■).

$$c = c_r + ic_i, \quad c_r = \mathrm{Re}(c), \quad c_i = \mathrm{Im}(c). \tag{66}$$

The propagation velocities c_p, the attenuation coefficient a_h, and the penetration depth h are determined by substituting the complex celerities c into Eq. (57):

$$c_p = \frac{|c|^2}{c_r}, \quad a_h = \frac{\omega c_i}{|c|^2}, \quad h = a_h^{-1}. \tag{67}$$

A. Results

1. Unimodal reconstructed porous media

The same samples as in Sec. IV C 1 were used to calculate the average effective moduli and dynamic permeability. Then, $c_\parallel$ and $c_\perp$ are derived. The dimensionless frequency ω'_Λ is given by (48) and the dimensionless celerity c' is defined as

$$c' = c\sqrt{\frac{\rho_f}{E_S}}. \tag{68}$$

The first important result is that the influence of ω'_Λ on $c_\parallel$ and $c_\perp$ is negligible (Fig. 10). In the low-frequency range, the celerities are constant and they slightly decrease when $\omega' > O(1)$; this corresponds to the phase change of the dynamic permeability (Sec. I) and consequently to the mode of wave propagation.

Figure 10 also shows that the celerities are decreasing functions of l_c/L. The difference between celerities for the same ϵ, but different l_c, is almost the same as for a dry pore space. For ϵ=0.15, the values of $c'_\parallel$ for l_c=6a and l_c=24a differ by 3.6%–4.6%. This difference increases with ϵ since it is about 7%–8% and 10%–11% for ϵ=0.2 and 0.3, respectively.

Figures 11(a) and 11(b) display the dimensionless penetration depths $h'=h/\Lambda$ as functions of ω'_Λ for all the media. In the low-frequency range, h is very large compared to Λ for both compressional and shear waves. $h_\perp/\Lambda$ does not depend on l_c. The dispersion of h observed in Fig. 11(a) can be attributed neither to l_c nor to ϵ. When represented as h/λ as a function of ω'_Λ, the same data are more dispersed than the previous ones; again, h is large compared to λ.

The second-degree equation (65) for $c_\parallel^2$ has two solutions. The second root corresponds to the slow and highly attenuated wave [2]. In Fig. 11(c), the slow wave celerities for various ϵ and l_c are plotted as functions of ω'_Λ. In the low-frequency range, the slow wave celerity increases as $\sqrt{\omega'_\Lambda}$ up to $\omega'_\Lambda = O(1)$. Its values for all the media are the same, except for l_c/L=3/8 with ϵ=0.15 and ϵ=0.2. Then, the behavior of this celerity changes for frequencies $\omega'_\Lambda > O(1)$. Three groups can be distinguished for each value of l_c. However, $c'_\parallel$ is independent of ϵ at high frequencies.

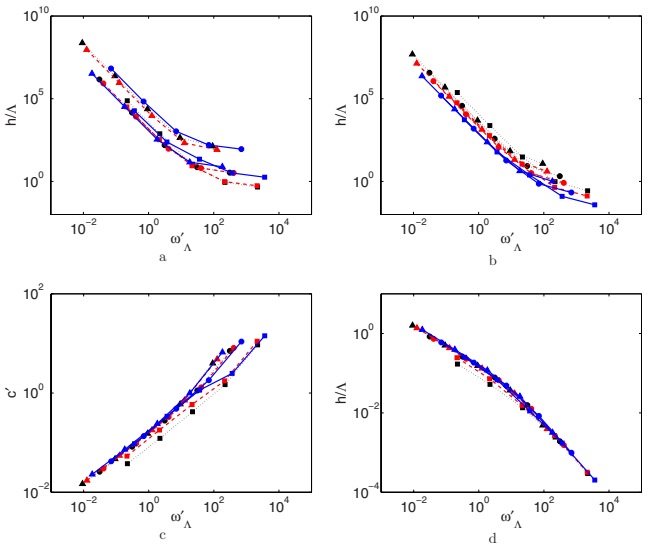

FIG. 11. (Color online) Unimodal media. The penetration depths h/Λ for the (a) compressional and (b) shear waves as functions of the frequency ω'_Λ. (c) The slow wave celerity $c'_\parallel$ as a function of the frequency ω'_Λ. (d) The penetration depth h/Λ for the slow wave as a function of ω'_Λ. Data are for ϵ=0.15 (black dotted line), 0.2 (red dashed line), and 0.3 (blue solid line); l_c/L=3/32 (▲), 3/16 (●), and 3/8 (■).

h for the slow wave is almost the same for all the media [Fig. 11(d)]. When represented in terms of h/λ, these data show that h is of the order of λ for low frequencies and then becomes smaller than λ for high frequencies.

2. Bimodal reconstructed porous media

The media are the same as the ones generated in Sec. IV C 2. In Figs. 12(a) and 12(b), the wave celerities are plotted as functions of ω'_Λ. In the low-frequency range, they are constant and do not depend on ω'_Λ. Then, the wave propagation mode is changed when $\omega'_\Lambda > O(1)$ as observed for the unimodal media (Fig. 10).

The celerities of the microporous medium HP with l_p =8a and of the vugular medium HV with l_v=32a differ by about 8%, while the celerities of the two bimodal media and of the unimodal medium HP are almost the same; i.e., the wave celerities are not influenced by the microstructure. Note that the total porosities are not exactly equal and that this may also influence the celerities.

Figures 12(c) and 12(d) show the influence of l_c on h. The results for the bimodal medium NPV and PV are the same, and their values are close to those for the microporous media. Again, $h_\parallel$ is different for the media HV and HP. However, in the low-frequency range, $h_\perp/\Lambda$ is similar for all

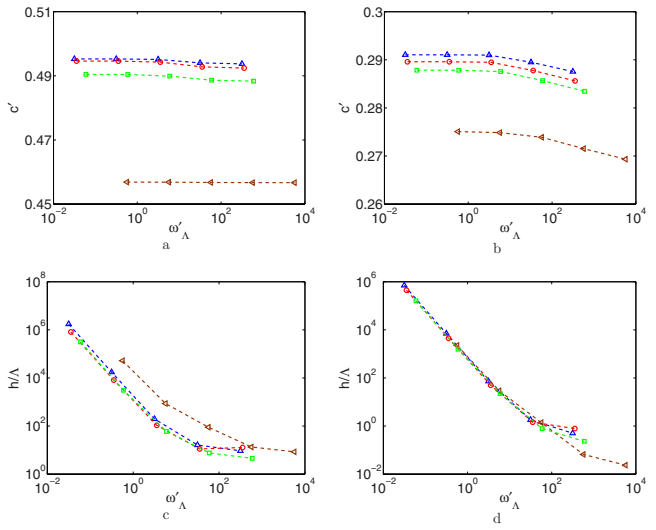

FIG. 12. (Color online) Bimodal media. (a) Compressional and (b) shear wave celerities c' as functions of the frequency ω'_Λ. The penetration depths h/Λ for the fast compressional (c) and shear (d) waves as functions of the frequency ω'_Λ. Data are for unimodal media HP (△) and HV (◁) and bimodal media NPV (○) and PV (□).

media. For the same data, the plots h/λ show that h for both compressional and shear waves is very large compared to λ; i.e., wave attenuation is negligible.

The slow wave celerities in the low-frequency range are almost the same for all media and the results are very close to Fig. 11(c). Moreover, h decreases with ω'_Λ and becomes small with respect to λ with results very similar to unimodal media.

3. Real porous media

The wave celerities are also determined for the sandstone and the carbonate described in Sec. IV C 3 for which Eq. (68) is applied with the modulus of the main solid component: namely, quartz and calcite, respectively. For all these media, the wave celerities do not depend on ω'_Λ as shown by Fig. 13(a). Moreover, $c_\perp$ is close for the two materials, while $c_\parallel$ is much larger for carbonate than for sandstone because of a smaller porosity.

The geometry has not much influence on h for both types of waves as seen in Fig. 13(b). h is much larger than λ [Fig. 13(c)] as observed for unimodal media.

For the slow wave, Fig. 14 shows that $c_\parallel$ and $h_\parallel$ are almost the same in the real sandstone and carbonate. As for the unimodal media, the regime changes for $\omega'_\Lambda = O(1)$. For low frequencies, the celerities are very small and they increase quickly for high frequencies. Since $h \ll \lambda$, the slow wave decays within distances smaller than λ.

But the whole theory is valid only if λ is much smaller than L according to Eq. (2). The same condition should be requested for h—i.e., $h \gg L$—for the result to be physically valid. If h is smaller or equal to L, its estimation is questionable.

B. Discussion

Various porous media were considered, and the influence of their microstructure on the wave celerities was analyzed.

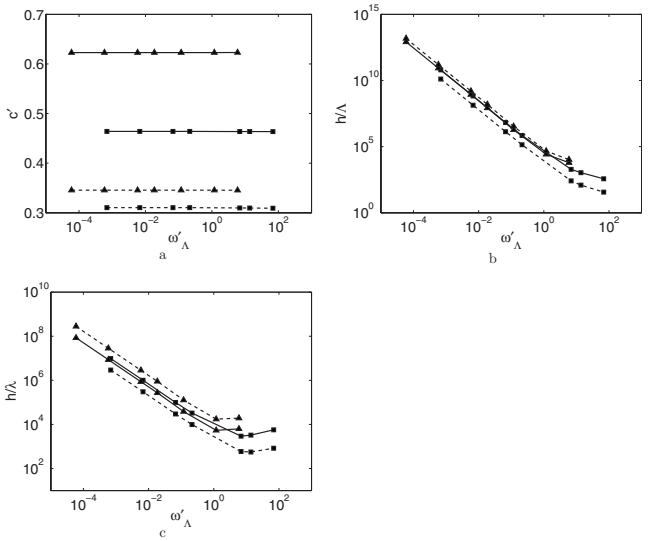

FIG. 13. Real porous media: $L/a=128$. (a) The compressional (solid line) and the shear (dashed line) wave celerities c' as functions of the frequency ω'_Λ for real sandstone (■) and real carbonate (▲). (b) The compressional (solid line) and shear (dashed line) wave penetration depths h/Λ as functions of the frequency ω'_Λ for the real sandstone (■) and for the real carbonate (▲). (c) The compressional (solid line) and the shear (dashed line) wave penetration depths compared to the wavelength h/λ as functions of the frequency ω'_Λ for the real sandstone (■) and for the real carbonate (▲).

For the slow wave, a unified description in terms of ω'_Λ is possible for all the media as shown by Fig. 15. In agreement with the predictions of [2], Fig. 15 shows that the slow wave celerity is a function of $\sqrt{\omega'_\Lambda}$ and that h is a function of $1/\sqrt{\omega'_\Lambda}$.

The fast compressional and the shear wave celerities for all the media almost do not depend on ω'_Λ and only small variations appear when $\omega'_\Lambda > O(1)$. The fast compressional and the shear wave celerities for the model media with $\nu = 0.275$ can be roughly approximated by linear fits [Fig. 16(a)]:

$$c'_\parallel = -0.7\epsilon + 0.7, \quad c'_\perp = -0.35\epsilon + 0.39. \tag{69}$$

For the real media, $c'_\perp$ follows well the fit (69) for both sandstone and carbonate [Fig. 16(a)]. $c_\parallel$ deviates more significantly from the fit (69). This may result from the hetero-

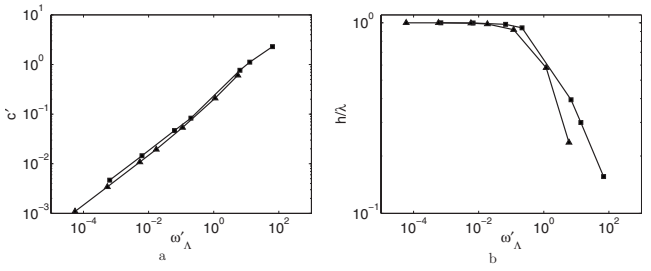

FIG. 14. The slow wave celerity $c'_\parallel$ (a) and its penetration depth compared to the wavelength h/λ (b) as functions of the frequency ω'_Λ for real sandstone (■) and real carbonate (▲); $L/a=128$.

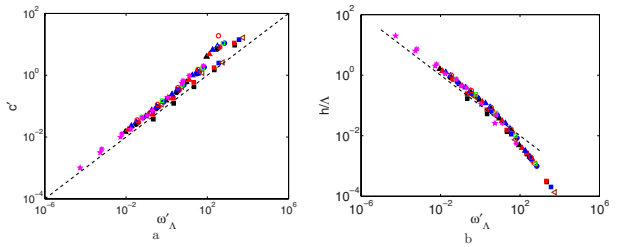

FIG. 15. (Color online) (a) The slow wave celerity $c'_{\parallel}$ and (b) its penetration depth compared to the wavelength h/λ as functions of the frequency ω'_{Λ}; $L/a=128$. The dashed lines in (a) and (b) correspond to $0.1\sqrt{\omega'}$ and to $0.1/\sqrt{\omega'}$, respectively. Data are for sandstone (∗), real carbonate (⋆), unimodal media HP (blue △) and HV (brown ◁), and bimodal media NPV (red ○) and PV (green □); unimodal reconstructed porous media with $l_c/a=6$ (▲), $l_c/a=12$ (●), and $l_c/a=24$ (■) and with $\epsilon=0.15$ (black), $\epsilon=0.2$ (red) and $\epsilon=0.3$ (blue).

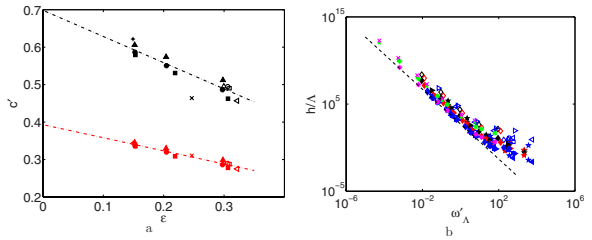

FIG. 16. (Color online) (a) The fast compressional (black) and the shear (red) wave celerity c' as functions of the porosity ϵ for the real sandstone (×) and for the real carbonate (+), for unimodal media HP (△) and HV (◁), bimodal media NPV (○) and PV (□), and unimodal media with $l_c/a=6$ (▲), $l_c/a=12$ (●), and $l_c/a=24$ (■). The dash-dotted lines correspond to the fits (69). (b) The penetration depth h/Λ for the compressional (open symbols) and the shear (solid symbols) waves as functions of ω'_{Λ} for unimodal media HP (blue △) and HV (brown ◁), and bimodal media NPV (red ○) and PV (green □); and unimodal reconstructed porous media with $l_c/a=6$ (◇), $l_c/a=12$ (▷), and $l_c/a=24$ (⋆) and with porosities $\epsilon=0.15$ (black), $\epsilon=0.2$ (red), and $\epsilon=0.3$ (blue), real sandstone (∗) and real carbonate (×) (where green and magenta symbols are for the compressional and shear waves, respectively. The dashed line corresponds to $500/\omega'^2$.

geneity of the solid properties, especially for the sandstone sample [see Fig. 4(c)].

The lengths h/Λ as functions of ω'_{Λ} for fast compressional and shear waves are almost the same for all media [Fig. 16(b)].

It has been demonstrated that the influence of the local geometry on the slow wave celerity and the penetration depth for all types of waves can be well taken into account by Λ, Eq. (47). The celerities of the fast compressional and shear waves do not depend on the frequency. It linearly increases when $\epsilon \to 0$ and varies with the microstructure. It should be noted that the foregoing results apply only as long as the scale separation condition (3) is satisfied. This implies

$$\omega' \ll \sqrt{\frac{\rho_f E_S \Lambda^2}{\mu_f^2}} \quad \text{or} \quad \omega \ll \sqrt{\frac{E_S}{\rho_f \Lambda^2}}. \tag{70}$$

With the parameters for the sandstone in Sec. VI A 3, the dimensional criterion reads $\omega \ll 10^8$ Hz, which entirely covers the practical range.

The importance of Λ can be commented and understood as follows. The definition (47) suggests that

$$\Lambda \approx \frac{2V_p}{S}, \tag{71}$$

where S is the fluid-solid interface and V_p the corresponding pore volume. In other words, Λ is proportional to the specific surface of the porous medium. This approximate relation has been verified by systematic calculations [19]. For high frequencies, the interaction zone between the fluid and solid is limited to a thin boundary layer. More precisely, the fluid motion in the pores is that of a potential flow except in a boundary layer of thickness $(\frac{2\mu}{\rho_f \omega})^{1/2}$ at the pore walls where the velocity goes to zero [8]. Therefore, the interaction is limited to the pore surface and it is likely that Λ plays a crucial role in the rationalization of the data. The important result of the present work is that this role is verified for complex three-dimensional structures and not only for elementary structures such as smooth or corrugated channels.

VII. CONCLUSIONS

The homogenization procedure is applied to the problem of wave propagation in porous media saturated with a Newtonian fluid. Three propagation modes are possible. The most general case is the biphasic mode from which the elastic mode can be easily derived. The viscoelastic mode was not considered here because it applies to very high frequencies and very small contrast between solid and fluid properties.

The local problems corresponding to the solid and fluid phases have been solved separately. The effective rigidity tensor and the effective coefficients $\boldsymbol{\alpha}$ and β were derived from the solution of the elastostatic equation in the solid with imposed macroscopic deformations or interstitial fluid pressure, respectively. The solution of the Navier-Stokes equation with imposed macroscopic pressure gradient yields the dynamic permeability tensor.

The elastic and transport characteristics of the various types of media were derived from the local problems and used to determine the global wave properties—namely, celerity and attenuation—in a systematic manner. To analyze the influence of the microstructure on the global results, model and real porous media have been used; to tackle such kinds of three dimensional media represents a significant progress with respect to the relatively simple media such as corrugated channels, which were addressed before. The resulting compressional and shear wave celerities do not depend on frequency. Substantial variations of the dynamic permeability with frequency were observed. However, these variations do not influence the wave celerities. The change of the attenuation coefficient behavior was observed on the same frequency range as phase change of the permeability.

The characteristic length Λ was successfully used to gather the results for the dynamic permeability as well as for the attenuation coefficients for all media; i.e., Λ fully

describes the influence of the microstructure on these results. This property, which can be interpreted in terms of the relation between Λ and the specific surface, is general and can be extended to other types of porous media.

ACKNOWLEDGMENTS

Most computations were performed at CINES (subsidized by the MENESR) whose support is gratefully acknowledged.

[1] F. Gassmann, Vierteljahrsschr. Natforsch. Ges. Zur. **96**, 1 (1951).
[2] M. A. Biot, J. Acoust. Soc. Am. **28**, 168 (1956).
[3] T. J. Plona, Appl. Phys. Lett. **36**, 259 (1980).
[4] J. L. Auriault and E. Sanchez-Palencia, J. Mec. **16**, 575 (1977).
[5] T. Lévy, Int. J. Eng. Sci. **17**, 1005 (1979).
[6] J. L. Auriault, Int. J. Eng. Sci. **18**, 775 (1980).
[7] C. Boutin and J. L. Auriault, Int. J. Eng. Sci. **28**, 1157 (1990).
[8] D. L. Johnson, J. Koplik, and R. Dashen, J. Fluid Mech. **176**, 379 (1987).
[9] P. Sheng and M. Y. Zhou, Phys. Rev. Lett. **61**, 1591 (1988).
[10] A. Cortis, D. M. J. Smeulders, J. L. Guermond, and D. Lafarge, Phys. Fluids **15**, 1766 (2003).
[11] I. Malinouskaya, I. Bogdanov, J.-F. Thovert, and P. M. Adler (unpublished).
[12] See EPAPS Document No. E-PLEEE8-77-016806 for supplementary material. For more information on EPAPS, see http://www.aip.org/pubservs/epaps.html.
[13] E. Sanchez-Palencia, *Non Homogeneous Media and Vibration Theory* (Springer-Verlag, Berlin, 1980).
[14] P. M. Adler, *Porous Media: Geometry and Transports* (Butterworth-Heinemann, Stoneham, 1992).
[15] D. L. Johnson, J. Koplik, and L. M. Schwartz, Phys. Rev. Lett. **57**, 2564 (1986).
[16] D. Coelho, M. Shapiro, J. F. Thovert, and P. M. Adler, J. Colloid Interface Sci. **181**, 169 (1996).
[17] C. G. Jacquin, Rev. Inst. Fr. Pet. **19**, 921 (1964).
[18] A. Moctezuma-Berthier, O. Vizika, and P. M. Adler, Transp. Porous Media **49**, 313 (2002).
[19] A. Valfouskaya, P. M. Adler, J.-F. Thovert, and M. Fleury, J. Appl. Phys. **97**, 083510 (2005).